



UNIVERSITY OF LEEDS

This is a repository copy of *Validation of a model of gas and dense phase CO jet releases for carbon capture and storage application*.

White Rose Research Online URL for this paper:
<http://eprints.whiterose.ac.uk/79569/>

Version: Accepted Version

Article:

Wareing, CJ, Fairweather, M, Woolley, RM et al. (1 more author) (2014) Validation of a model of gas and dense phase CO jet releases for carbon capture and storage application. *International Journal of Greenhouse Gas Control*, 20. 254 - 271. ISSN 1750-5836

<https://doi.org/10.1016/j.ijggc.2013.11.012>

Reuse

Unless indicated otherwise, fulltext items are protected by copyright with all rights reserved. The copyright exception in section 29 of the Copyright, Designs and Patents Act 1988 allows the making of a single copy solely for the purpose of non-commercial research or private study within the limits of fair dealing. The publisher or other rights-holder may allow further reproduction and re-use of this version - refer to the White Rose Research Online record for this item. Where records identify the publisher as the copyright holder, users can verify any specific terms of use on the publisher's website.

Takedown

If you consider content in White Rose Research Online to be in breach of UK law, please notify us by emailing eprints@whiterose.ac.uk including the URL of the record and the reason for the withdrawal request.



eprints@whiterose.ac.uk
<https://eprints.whiterose.ac.uk/>

Validation of a model of gas and dense phase CO₂ jet releases for carbon capture and storage application

Christopher J. Wareing^{a,*}, Michael Fairweather^a, Samuel A.E.G. Falle^b,
Robert M. Woolley^a

^a*School of Process, Environmental and Materials Engineering, University of Leeds, Leeds LS2 9JT, UK.*

^b*School of Mathematics, University of Leeds, Leeds LS2 9JT, UK.*

Abstract

Carbon capture and storage (CCS) presents a short-term option for significantly reducing the amount of carbon dioxide (CO₂) released into the atmosphere and mitigating the effects of climate change. To this end, National Grid initiated a programme of research known as the COOLTRANS research programme. Part of this work involves the development of a mathematical model for predicting the near-field dispersion of CO₂ following the puncture or rupture of a high pressure dense phase pipeline typical of those planned for transport usage in CCS. This article describes the validation of such a model against experimental data on dense phase and gas phase releases from high pressure pipes above ground. The two-component CO₂ and air model has proved capable of accurately predicting the near-field dispersing structure of such releases, including the core and radial temperatures within the sonic jets formed. This has required a three-phase accurate equation of state

*Corresponding author. Tel: +44 113 343 1619. Fax: +44 113 343 5090

Email address: C.J.Wareing@leeds.ac.uk (Christopher J. Wareing)

URL: <http://www.maths.leeds.ac.uk/~cjlw> (Christopher J. Wareing)

for pure CO₂, that also accounts for the latent heat of fusion, as well as a homogeneous relaxation model to allow the modelling of non-equilibrium conditions. The work described demonstrates the capability of the model to provide accurate predictions in the shock-containing near-field region. It provides the basis for developing robust pseudo source conditions for use in CFD studies of far-field dispersion and for use with the pragmatic models used in quantified risk analysis.

Keywords: CCS, multi-phase flow, experimental measurement, mathematical modelling, accidental releases, atmospheric dispersion

1. Introduction

Carbon capture and storage (CCS) refers to a set of technologies designed to reduce carbon dioxide (CO₂) emissions from large point sources of emission, such as coal-fired power stations, in order mitigate greenhouse gas production. The technology involves capturing CO₂ and then storing it in a reservoir (sequestration), instead of allowing its release to the atmosphere, where it contributes to climate change. Once captured, the CO₂ is transported and sequestered, typically underground, or used for processes such as enhanced oil recovery.

National Grid has initiated the TRANSportation of Liquid CO₂ research programme (COOLTRANS) (Cooper, 2012) in order to address knowledge gaps relating to the safe design and operation of onshore pipelines for transporting dense phase CO₂ from industrial emitters in the UK to storage sites offshore. This includes developing the capability for modelling accidental releases from a buried pipeline that contains CO₂ in the dense phase and

applying the learning from these studies to develop an appropriate quantified risk assessment (QRA) for a dense phase CO₂ pipeline. The programme includes theoretical studies by University College London (UCL), the University of Leeds and Kingston University, carried out in parallel to provide “state of the art” models for the outflow, near-field dispersion behaviour and far-field dispersion behaviour associated with below ground CO₂ pipelines that are ruptured or punctured. Experimental work and studies using currently available practical models for risk assessment are being carried out by Germanischer Lloyd Noble Denton (GLND) (Allason et al., 2012).

In this paper, experimental results from a gas phase release and a dense phase release are compared to simulations, validating the numerical approach developed for modelling this type of above ground release (Wareing et al., 2012, 2013; Woolley et al., 2013). This paper represents a step toward the goal of developing the understanding and modelling capabilities for below ground releases by considering the case of a free jet emerging into the atmosphere through a purpose designed vent. In addition, the cases are of interest in their own right as they may apply directly to certain planned venting operations. In the next section, previous work of relevance to this study is reviewed. Experimental details, including the rig, instrumentation and test procedure are then discussed. The numerical simulations, including details of the numerical model, are presented in Section 4. Comparisons of the predictions and the experimental data are presented and analysed in Section 5. A discussion of the implications of these results is given in Section 6, followed by conclusions in Section 7. Throughout this work, references to the “near-field” indicate those parts of the flow in which the pressure is relaxing

to its atmospheric value immediately downstream of the release. This region typically contains a Mach shock structure, with associated rapid changes in velocity, temperature and phase of the CO₂. References to the “far-field” indicate the regions beyond the Mach shock where the pressure is atmospheric. We consider the far-field up to where the nearest experimental measurements of temperature have been made.

It should also be noted that the modelling work presented here has further possible applications, and not solely within the field of CO₂ pipeline safety. The representation of the three-phase CO₂ expansion and the associated thermo-physical phenomena is a novel approach. This could be applied in a number of areas of technology including those based upon the Rapid Expansion of Supercritical Solvents (RESS) processes including pharmaceutical, cosmetic, and speciality chemical industries. In these applications, the geometry of particles produced is determined by a number of factors including nozzle geometry, mass flow-rate, and pressure and temperature of CO₂. Hence, an ability to model and predict fluid structures (such as Mach shock positions and widths as well as jet characteristics and dimensions) and particle distributions would be a great benefit in the design stage of such processes.

2. Literature review

A growing number of recent publications have examined the release and dispersion of CO₂, summarised in depth by Dixon et al. (2012). We abridge and summarise here recent work relevant to the prediction of near-field conditions.

A study by MMI Engineering (Dixon and Hasson, 2007) presented dispersion simulations employing the ANSYS-CFX computational fluid dynamics (CFD) code. Solid CO₂ particles were simulated by a scalar representing the particle concentration, in order to avoid additional computing associated with Lagrangian particle tracking. Dixon et al. (2012) note that this method assumed a constant particle diameter and temperature (at the sublimation temperature of 194.25 K) in order to calculate heat and mass exchange between the particles and the gas phase. In a following publication (Dixon et al., 2009), particles were modelled via a Lagrangian particle tracking method, but were still assumed to be at the sublimation temperature. Dixon et al. (2012) note that since the rate of sublimation increases as particle size decreases, an improved distribution of the source of the CO₂ gas resulting from particle sublimation could be obtained by allowing for varying particle size and for the fact that temperature is expected to fall below the sublimation temperature in the near-field of a release.

In 2011, Webber (2011) presented a methodology for extending existing two-phase homogeneous integral models for flashing jets to the three-phase case for CO₂. Webber noted that as the flow expands from the reservoir conditions to atmospheric pressure, temperature, density and the jet cross-sectional area would vary continuously through the triple point, whilst the mass and momentum would be conserved. This led to the conclusion that there must be a discontinuity in the enthalpy and CO₂ condensed phase fraction, in a similar manner to the energy change associated with passing through a hydraulic jump. In the development of our composite equation of state for modelling CO₂ near-field sonic dispersion (Wareing et al., 2012,

2013), we confirmed this in a conservative shock capturing CFD code and highlighted the importance of fully accounting for the solid phase and latent heat of fusion; the near-field structure of the jet as well as the fraction of solid phase material is different when this is correctly accounted for.

Two recent papers (Witlox et al., 2009, 2011) have discussed the application of the software package PHAST to CO₂ release and dispersion modelling. In the first of these, Witlox et al. (2009) described an extension to the existing model in PHAST (v. 6.53.1) to account for the effects of solid CO₂, including the latent heat of fusion. The modifications to the model consisted principally of changing the way in which equilibrium conditions were calculated in the expansion of CO₂ to atmospheric pressure. This was done in order to ensure that below the triple point, conditions followed the sublimation curve in the phase diagram, rather than extrapolating the evaporation curve (which diverges considerably from reality, hence the limitations of the Peng and Robinson (1976) and Span and Wagner (1996) equations of state to above the triple point only). In the second paper (Witlox et al., 2011), the results of sensitivity tests were reported for both liquid and supercritical CO₂ releases from vessels and pipes calculated with the revised PHAST model. The public release of the CO2PIPETRANS datasets and associated industrial reports has validated the development of this approach, which we have also adopted in part for our composite equation of state.

E.ON have published a number of studies in support of their proposed CCS programme (Mazzoldi et al., 2008a,b, 2011; Hill et al., 2011). Of these, the most relevant to this work are Mazzoldi et al. (2011) and Hill et al. (2011). These consider atmospheric dispersion from pipeline and vessel releases. The

former paper compared simulations from the heavy gas model ALOHA to the CFD model Fluidyn-Panache. Only the gaseous stage of the release was modelled. In the second work (Hill et al., 2011), the authors presented CFD and PHAST simulations of dense-phase CO₂ releases from a 0.5m diameter hole in a pipeline, located at an elevation of 5m above level ground. Steady-state flow rates were calculated at the orifice assuming saturated conditions. CFD simulations were performed using the ANSYS-CFX code with a Lagrangian particle tracking model for the solid CO₂ particles, with three size distributions: 10 to 50 micrometers, 50 to 100 micrometers and 50 to 150 micrometers. Simulations were also performed without particles. Their results showed that sublimation of the particles led to a cooling of the CO₂ plume, affecting dispersion behaviour, although the results were relatively insensitive to particle size. Gas concentrations downwind from the release were reportedly somewhat lower using PHAST (v 6.6) as compared to the CFD results. No comparison to experiment was performed.

Dixon et al. (2012) point out that it appears that in the Lagrangian model of Hill et al. (2011) their particle tracks followed closely the plume centre-line, rather than being spread throughout the plume. Dixon et al. (2012) noted that turbulence will have the effect of bringing particles into contact with parts of the jet at a higher temperature and lower CO₂ concentration, thereby tending to increase the rate of sublimation and increase the radius of the region cooled by the subliming particles. In their work, Dixon et al. (2012) included turbulent dispersion effects in the CFX model. Further, they assumed that the solid particles are much smaller with an initial particle diameter of 5 micrometers. They made that choice based on an analysis of

CO₂ experiments. In addition, this particle size distribution is supported by the model recently developed by Hulsbosch-Dam et al. (2012b,a), which suggested that the particle diameter would be around 5 micrometers for CO₂ releases at a pressure of 100bar, when the difference between the CO₂ and ambient temperatures is around 80°C. They stated that the effect of having smaller particles in their model was likely to cause more rapid sublimation, which should produce a more significant reduction in gas temperature in the jet. Recent examination of particle size distribution in releases of supercritical CO₂ from high pressure has shown that even smaller particles immediately post Mach shock are indeed the case (Liu et al., 2012b), on the order of a few micrometers.

Dixon et al. (2012) employ a Bernoulli method in their recent paper which they found "to provide reasonable predictions of the flow rate for the sub-cooled liquid CO₂ releases". Differences were apparent between the integral model and the CFD model results. The integral model predicted temperatures that they noted were too low in the near-field, and which then returned too rapidly to atmospheric levels (see Dixon et al. (2012) Figure 3.). The CFD model was noted to be in general better, although in the very near-field (< 10m from the orifice) it was still not clear whether this was the case. Further, the CFD model appears to under-predict the spreading rate of the jet.

It is with the intention of providing accurate conditions in the jet once it has expanded to atmospheric pressure that the model described here has been developed, together with its validation. In this section, a number of improvements have been identified which should be considered in developing

a more accurate near-field model, to ensure that a robust pseudo source for far-field predictions is developed for the prediction of the hazard associated with far-field dispersion and for use with the pragmatic models used in quantified risk analysis. Of those improvements and developments, in this work we employ a more accurate composite equation of state and an improved (compressibility-corrected) turbulence model and demonstrate the benefits of these improvements through validation against data on CO₂ releases.

3. Experimental details

Experiments were carried out by GLND (Allason et al., 2012), under instruction from National Grid as part of the COOLTRANS programme of research (Cooper, 2012) in order to study the venting of dense phase CO₂ through a single, straight vertical vent pipe of constant diameter. The configuration was arranged so that an approximately steady flow was produced through the vent pipe for a minimum period of 30 seconds. The experiments were performed at the GLND Spadeadam facility in Cumbria, U.K. We summarise the relevant details of the experimental rig, installation and test procedure in the rest of this section.

3.1. *Experimental Rig*

The rig consisted of the following four main components: a buffer pipe, a main CO₂ storage vessel, a supply pipe and a vent pipe. The buffer pipe was a 0.15m internal diameter pipe of 132m length that sloped downwards from its connection with a high pressure nitrogen reservoir at the upper end to the CO₂ storage vessel at the other end. The CO₂ storage vessel was a 0.6m diameter horizontal vessel of 24m in length. It could be filled independently

from a large refrigerated CO₂ storage vessel or from the buffer pipe. The supply pipe was a horizontal pipe of 0.05m diameter and 12m length that was connected to the main storage vessel at one end by a flexible pipe and, having turned through 90 degrees at an elbow, to the vertical vent pipe at its other end. The vent pipe was a length of 0.0243m internal diameter pipe that was connected to the supply pipe at one end and was open to the atmosphere at the other end. The top of the vent pipe can be located at 3m or 5m above the ground. In the cases considered in this work, it was located 3m above ground. An outline drawing of the experimental rig is given in Figure 1. A photograph of the vent pipe and associated supports is shown in the left panel of Figure 2.

3.2. Instrumentation

A number of temperature and pressure measurements were made in the buffer pipe and the supply vessel in order to monitor the experiments. A Coriolis flow meter was installed in the horizontal section of the supply pipe. The pressure and temperature of the fluid was measured in the supply pipe at two locations 9m apart. The pressure and fluid temperature near to the base and near to the exit of the vent pipe were measured. The vent pipe was connected to the supply pipe at its base. The vent pipe itself was Schedule 80 steel, with an internal diameter of 0.0243m and wall thickness of 4.55×10^{-3} m. The roughness of the pipe was measured and found to be 0.5×10^{-6} m.

Above the vent exit, measurements of the temperature in the releases were taken on two horizontal planes at 7m and 10m above ground, that being 4m and 7m above the vent exit for the experiments reported here, and perpendicular to the release direction. Thermocouples were attached

to suspended frames on these planes, as illustrated in Figure 3 and shown photographically during a test release in the right panel of Figure 2. The location of the thermocouples within the arrays is detailed in Figures 4 and 5. The centre of each array was aligned with the release axis in order to measure the core temperature in the jet.

3.3. Test Procedure

The buffer pipe, storage vessel and supply pipe to the vent were filled with CO₂ to a pressure of 15 MPa for the dense phase test and to a pressure of 3.55 MPa for the gas phase test prior to an experiment taking place. After checks had been made on the conditions in the system, a trigger was sent from the remote control room to open the valve in the supply pipe to allow flow into the vent pipe and to start recording the temperature data. The test proceeded for a preset period, during which quasi-steady conditions were established in the flow path. This period was set so that the nitrogen used to maintain the pressure in the storage vessel did not enter the storage vessel from the buffer pipe during the data collection period. Maintaining the pressure in the storage vessel sustained the approximation to the initial stages of venting a high-pressure CO₂ pipeline such as intended for CCS transport scenarios in the U.K. Appropriate valves in the vent pipe and buffer pipe were closed to terminate the flow.

The reservoir conditions from GLND are listed in Table 1 as well as the vent exit conditions calculated by the model described below for the gas phase test and by University College London for the dense phase test (H. Mahgerefteh, private communication as part of the COOLTRANS programme (Cooper, 2012)). The dense phase predictions from UCL are in

agreement with predictions from our model described below. The predicted mass-flow rate (\dot{m}_i) is

$$\dot{m}_i = \pi \left[\frac{D}{2} \right]^2 u_i \rho_i \quad (1)$$

where D is the vent pipe diameter, u_i is the release velocity at the end of the vent pipe and ρ_i is the density, where for CO₂ fraction $\beta_i = 1$,

$$\rho_i = \frac{1}{\left(\frac{\alpha_i}{\rho_l} + \frac{1-\alpha_i}{\rho_g} \right)}. \quad (2)$$

where α_i is the condensed phase fraction, ρ_l the condensed phase density and ρ_g the gas phase density. The mass-flow rate was set to $\dot{m}_i = 41 \text{ kg s}^{-1}$ for the dense phase test, based on the mass-flow experimentally measured by the Coriolis flow meter installed in the horizontal section of the supply pipe.

Consistent measurements of temperature were obtained on the two planes above the vent at 4m (165 vent diameters (D)) and 7m (288D) and it is to these data that the model performance has been compared. The experimental data has a variance on each measurement during the relevant time period of a degree or two. The temperature sensors are accurate over this range to within ± 5 degrees Celsius at worst, hence throughout all the plots given later the experimental measurements are plotted with 5 degree error bars, although this is considerably larger than the degree or two variance of the measurement of the relevant steady state time period of the jet (from 10 to 40 seconds into the release). The plotted temperature is the simple average for that particular sensor during the steady state period. The response time of the sensors is certainly less than the steady state period. From the sensor traces, it is possible to estimate that the response time to reach 80% of the temperature change is up to 5 seconds. Going from cold to hot following

the release is considerably longer, due to possible ice formation around the connections, but this is beyond the steady-state period.

4. Numerical modelling

4.1. Reynolds-Averaged Navier-Stokes Model

The Reynolds-averaged Navier-Stokes (RANS) equations, closed with a compressibility-corrected k- ϵ turbulence model, employed in this work are:

$$\frac{\partial \rho}{\partial t} + \nabla \cdot (\rho \mathbf{u}) = 0 \quad (3)$$

$$\frac{\partial \rho C}{\partial t} + \nabla \cdot (\rho C \mathbf{u}) - \nabla \cdot (\mu_T \nabla C) = 0 \quad (4)$$

$$\frac{\partial \rho \mathbf{u}}{\partial t} + \nabla \cdot (\rho \mathbf{u} \mathbf{u}) + \nabla P - \nabla \cdot \boldsymbol{\tau} = \mathbf{s}_p \quad (5)$$

$$\frac{\partial E}{\partial t} + \nabla \cdot [(E + P) \mathbf{u} - \mathbf{u} \cdot \boldsymbol{\tau}] - \nabla \cdot (\mu_T T \nabla S) = 0 \quad (6)$$

$$\frac{\partial \rho k}{\partial t} + \nabla \cdot (\rho k \mathbf{u}) - \nabla \cdot (\mu_T \nabla k) = s_k \quad (7)$$

$$\frac{\partial \rho \epsilon}{\partial t} + \nabla \cdot (\rho \epsilon \mathbf{u}) - \nabla \cdot (\mu_\epsilon \nabla \epsilon) = s_\epsilon \quad (8)$$

where the variables have their usual meanings, noting that the vector velocity is expressed in bold as \mathbf{u} and S is the entropy per unit mass. The turbulent diffusion coefficients are

$$\mu_T = \rho C_\mu \frac{k^2}{\epsilon}, \quad \mu_\epsilon = \frac{\mu_T}{1.3}, \quad C_\mu = 0.09. \quad (9)$$

The turbulence production term is

$$P_t = \mu_T \left[\frac{\partial u_i}{\partial x_j} \left(\frac{\partial u_i}{\partial x_j} + \frac{\partial u_j}{\partial x_i} \right) \right] - \frac{2}{3} \nabla \cdot \mathbf{u} (\rho k + \mu_T \nabla \cdot \mathbf{u}), \quad (10)$$

where the summation convention has been assumed. In axisymmetry, the production term is as above with an extra geometric term

$$2\mu_T \frac{u_r^2}{r^2}. \quad (11)$$

The momentum equation source term, \mathbf{s}_p , is zero in Cartesian coordinates. In axisymmetry it is

$$\mathbf{s}_p = \begin{pmatrix} \mu_T \left[\frac{2}{3r} \nabla \cdot \mathbf{u} - 2 \frac{u_r}{r^2} \right] + \frac{1}{r} \left[P + \frac{2}{3r} \rho k \right] \\ 0 \end{pmatrix}. \quad (12)$$

The k source term is

$$s_k = P_t - \rho \epsilon \quad (13)$$

whilst the ϵ source term is

$$s_\epsilon = \frac{\epsilon}{k} (C_1 P_t - C_2 \rho \epsilon), \quad C_1 = 1.4, \quad C_2 = 1.94. \quad (14)$$

The turbulent stress tensor, τ , is

$$\tau_{ij} = \mu_T \left(\frac{\partial u_i}{\partial x_j} + \frac{\partial u_j}{\partial x_i} \right) - \frac{2}{3} \delta_{ij} (\mu_T \nabla \cdot \mathbf{u} + \rho k). \quad (15)$$

The k- ϵ turbulence model described here is coupled to a compressibility dissipation rate correction proposed by Sarkar et al. (1991). Comparisons of model predictions with this correction and experimental data have shown significant improvements over results derived using the standard k- ϵ approach for moderately and highly under-expanded jets of the variety under consideration here (Cumber et al., 1994, 1995).

4.2. Equation of State

The composite equation of state for pure phase properties recently described by Wareing et al. (2012, 2013) is employed. This composite method predicts the thermophysical properties of the three phases of CO₂ for the range of temperatures of relevance to carbon dioxide dispersion from releases at sonic velocities, of interest to the carbon, capture and storage industry. This new equation of state has been developed in such a way that is convenient for computational fluid dynamic applications; the gas phase is computed from the Peng-Robinson equation of state (Peng and Robinson, 1976), and the liquid and condensed phases from tabulated data generated with the Span & Wagner equation of state (Span and Wagner, 1996) and the DIPPR[®] Project 801 database. Saturation pressure, gas and condensed phase densities, sound speed and internal energy have all been tabulated against temperature, providing the basis for a fully functional form for differentiation, interpolation and extrapolation in numerical simulations. No discontinuity or loss of accuracy at the critical point or anywhere along the saturation curve has been encountered by using this composite approach with different equations of state, as the authors have ensured that the Helmholtz free energy has continuous first derivatives.

The authors examined predictions of a free release of CO₂ into the atmosphere from a reservoir at a pressure of 10 MPa and a temperature of 10 degC, typical of transport conditions in carbon capture and storage scenarios. They performed inviscid RANS calculations employing three approaches: an ideal equation of state; the two-phase Peng-Robinson equation of state; and the new composite three-phase method. A comparison of the results (Wareing

et al., 2012, 2013) showed that the sonic CO₂ jet that formed required a three-phase equation of state including the latent heat of fusion to realistically simulate its characteristics. The characteristics of the Mach shock are considerably different between a two-phase accurate approach and the new more accurate three-phase accurate composite approach. Further, the fraction of solid CO₂ is considerably different in the more accurate three-phase approach, implying the correct modelling of this phase may be important for safety considerations in CCS transport scenarios.

4.3. Homogeneous Relaxation Model

The computational implementation assumes that the mixture is in homogeneous equilibrium, i.e. that the solid/liquid and gas phases are well mixed and that the liquid drops or solid particles are sufficiently small. There are indications from recent experimental work that this will not be true, in particular for test calculations in which the release size is of the order of centimetres (Liu et al., 2012a) or less.

A full model would require the inclusion of non-equilibrium drops or particles and modelling of particle evolution including nucleation, agglomeration and evaporation/condensation as well as the Kelvin effect. This is beyond the scope of the present work, but an improved model is in development. For the current model, a simple sub-model for the relaxation to equilibrium has been included, in which the temperature relaxation is ignored and the condensed phase mass fraction is simply given by

$$\frac{\partial \rho \alpha}{\partial t} + \nabla \cdot (\rho \alpha \mathbf{u}) - \nabla \cdot (\mu_T \nabla \alpha) = S_\alpha. \quad (16)$$

The source term is then

$$S_\alpha = \beta \frac{(p_v - p_s)}{\tau p_s} \quad (17)$$

where p_v is the vapour pressure, p_s is the saturation pressure and τ is a relaxation time. This is consistent with the standard textbook form of evaporation/condensation rate, for example given by Jacobson (1999). Our method is developed according to Jacobson (1999). In the model, it allows the gas temperature to vary from the sublimation temperature at atmospheric pressure when the solid phase is present in the flow.

4.4. Implementation

Following the same method as used previously (Wareing et al., 2012, 2013), the composite equation of state was implemented into MG, an adaptive mesh refinement (AMR) Reynolds-averaged Navier-Stokes hydrodynamic code developed by Falle (1991). The code employs an upwind, conservative shock-capturing scheme and is able to employ multiple processors through parallelisation with the message passing interface (MPI) library. Integration in space proceeds according to a second-order accurate Godunov method (Godunov, 1959). In this case, a Harten Lax van-Leer (van Leer, 1977; Harten et al., 1983) (HLL) Riemann solver was employed to aid the implementation of complex equations of state. The disadvantage of the HLL solver is that it is more diffusive for contact discontinuities; this is not important here since the contact discontinuities are in any case diffused by the artificial viscosity. The artificial viscosity is required to ensure shocks travel at the correct speed in all directions and is at a very low level, decreasing proportionally with increasing resolution.

4.5. Adaptive meshing strategy

The AMR method (Falle, 2005) employs an unstructured grid approach, requiring an order of magnitude less memory and giving an order of magnitude faster computation times than structured grid AMR. The two coarsest levels - 0 and 1 - cover the whole computational domain; finer grids need not do so. Refinement or derefinement depends on a given tolerance. Where there are steep gradients of variable magnitudes such as at flow boundaries or discontinuities such as the Mach disc, this automated meshing strategy allows the mesh to be more refined than in areas of the free stream in the surrounding fluid. Each layer is generated from its predecessor by doubling the number of computational cells in each spatial direction. This technique enables the generation of fine grids in regions of high spatial and temporal variation, and conversely, relatively coarse grids where the flow field is numerically smooth. Defragmentation of the AMR grid in hardware memory was performed at every time-step, gaining further speed improvements for negligible cost through reallocation of cells into consecutive memory locations. The simulations performed employed an artificial viscosity dependent on grid resolution also in order to avoid numerical instabilities. This viscosity decreases with the maximum number of AMR levels employed. The simulations presented below employed 4 levels of AMR and hence a low level of artificial viscosity. Steady state was achieved through starting simulations at the coarsest level and establishing a steady state before adding another grid level and again advancing in time with the same constant exit conditions until steady state was again achieved. The simulations shown below are convergent and show little variation with exit pressure, temperature and

velocity.

4.6. Initial Conditions

In computationally simulating the releases considered below, we have employed a two-dimensional cylindrical polar axisymmetric coordinate system. Numerical simulations were performed employing the vent exit conditions listed in Table 1 as input conditions in the region defined by $r < 0.5$ (dimensions are scaled by the vent exit diameter) on the $z = 0$ boundary. The initial state of the fluid in the domain consists entirely of stationary air at a pressure and temperature given in Table 1. Conditions in air are calculated via an ideal gas equation of state with $\gamma_a = 7/5$. The near-field Mach shock structure was simulated in one run and then conditions shortly after the Mach shock (at 15D) but away from any boundary effects were taken as the input for a larger grid simulating out to the measurement planes. The $r = 0$ axis was treated as symmetric and the other r boundary as free flow, introducing air with the initial atmospheric condition if an in-flow was detected. This neglects the effects of a cross-flow in the atmosphere, but is a reasonable approximation to make over this range, where the momentum from the release is expected to dominate. The $z = 0$ axis was fixed by the input conditions for $r < 0.5$ and as a solid wall outside this region, ignoring any ability of the release to entrain air from beneath the vent tip for the purposes of this work. The other z axis was free-flow, again only allowing the in-flow of air with the initial atmospheric condition if in-flow was detected, for example as a result of vortices formed before the jet reaches steady state. Given that vortex structures may be present in the jet as it reaches steady state, velocities that lead to inflow can occur at the free-flow boundaries.

Hence the boundary conditions are adjusted to ensure that only ambient air can flow into the domain, with the same properties as the initial condition, and no CO₂. The exit conditions in Table 1 are enforced on every step at the $z = 0$ boundary for $r < 0.5$. At this time we have not included humidity in the models. We discuss the implications of this in later sections.

5. Results

5.1. Data Representation

A number of results from the simulations, including a number of different line graphs and two-dimensional contour plots, are presented. Firstly, comparisons of the model predictions with the experimental data are given. These figures contain four plots to show the four different quadrants of the measurement array, defined by compass direction. Hence the plots show north at the top, south at the bottom, east at middle right and west at middle left. The “north” quadrant (top row) shows predictions and the experimental data from the sensors in a 90 degree sector from 315 degrees east of north (north-west) to 45 degrees east of north (north-east), through north itself (0 degrees). The “east” quadrant (middle row, right) shows predictions and the experimental data from the sensors in a 90 degree sector from north-east (45 degrees east of north) to south-east (135 degrees east of north). The “south” quadrant (bottom row) shows predictions and the experimental data from the sensors in a 90 degree sector from south-east (135 degrees east of north) to south-west (225 degrees east of north). The “west” quadrant (middle row, left) shows predictions and the experimental data from the sensors in a 90 degree sector from south-west (225 degrees east of north) to north-

west (315 degrees east of north). The data have been plotted in this way in order to elucidate any atmospheric effects on the experimental data caused by a cross-wind. Both tests were carried out with a cross-wind blowing from approximately 245 degrees \pm 10 degrees (west south west) at an average of 2.5 m s⁻¹. The “east” quadrant experimental data are therefore least likely to be affected by a compression towards the axis from the cross-wind. However, other effects may change the jet through, e.g., turbulent vortex effects at its edges, which may mean that this quadrant is sometimes affected by atmospheric effects. It should also be noted that some experimental data points appear twice, at $x = 0.575\text{m}$ in the 4m plane figures and $x = 1.133\text{m}$ in the 7m plane figures. This is because those individual sensors are on the north-east, south-east, south-west and north-west directional lines. All the other data points are purely in the north, south, east and west directions, so the experimental data at $x = 0.575\text{m}$ for the 4m plane and $x = 1.133\text{m}$ for the 7m plane can be ignored in order to select the experimental data in a single compass direction north, south, east or west. Model predictions are the same between all four plots (as the simulation employs symmetry about the vertical axis). Typically several predictions are given, showing those from the homogeneous equilibrium model and those from the homogeneous relaxation model going out of equilibrium to varying degrees (i.e. increasing values of the relaxation time τ).

Secondly, predictions of the conditions along the centreline of the jet from the release point, through the Mach shock in the near-field and into the far-field, are shown. The centreline temperature (top left), mean velocity (top right), fraction of CO₂ (middle left), fraction of CO₂ in the solid

phase (middle right) and the pressure (bottom row), which typically reaches atmospheric immediately after the shock, are plotted.

Thirdly, two-dimensional colour plots of the conditions in the near-field are shown, defined as the region containing the Mach shock structure up to approximately 10 vent exit diameters from the vent exit. These figures include the temperature (top left), logarithm to base 10 of the pressure (top right), mean velocity (middle left), logarithm to base 10 of the density (middle right), CO₂ fraction (bottom left) and fraction of CO₂ in the solid phase (bottom right). For the gas phase test, the fraction of CO₂ in the solid phase is not shown as calculations show it is zero in the entire flow domain.

Finally, two-dimensional colour plots of the conditions in the far-field are shown, typically the region beyond 15 to 20 vent exit diameters from the vent exit where pressure is at atmospheric levels across the entire region. These figures include the temperature (top left), mean velocity (top right), CO₂ fraction (middle left), fraction of CO₂ in the solid phase (middle right) and linear plot of density (bottom row). Pressure is not shown as it is constantly atmospheric to within 1% over the entire domain. For the gas phase test, the fraction of CO₂ in the solid phase is again not shown as it is zero in the entire flow domain.

5.2. Dense Phase Test

5.2.1. 4m measurement plane

Figure 6 shows the model predictions and the experimental measurements at the measuring plane 4m (165 vent diameters) above the vent exit for the dense phase test. Model predictions are shown from the homogeneous equilibrium model (dotted line) and the homogeneous relaxation model with

$\tau = 10$ (dashed line) and $\tau = 100$ (solid line). When scaled into seconds, these correspond to relaxation times of 0.25 seconds and 2.5 seconds, respectively. Whilst all three models predict the temperature of the jet on the centreline (or core) reasonably well, it is clear that the relaxation model fits the data outside the core more accurately. The experimental data show no clear evidence of atmospheric effects when plotted in this way - all four plots looks similar. The predicted width of the jet around 1m is also consistent with estimations from photographs of the experiment. The experimental measurement at 0.8m in the North quadrant (top row) would appear to be inconsistent with the other three measurements at 0.8m from the other quadrants and may be suspect. As a result, this measurement has been ignored.

5.2.2. 7m measurement plane

Figure 7 shows the model predictions and the experimental measurements at the measuring plane 7m (288 vent diameters) above the vent exit. Model predictions are again shown from the homogeneous equilibrium model (dotted line) and the homogeneous relaxation model with $\tau = 10$ (dashed line) and $\tau = 100$ (solid line). At this distance from the vent exit, which is considerably further from the Mach shock and hence into the far-field, the equilibrium model under-predicts the core temperature by more than 20 degrees. By employing a homogeneous relaxation model, the core temperature is fitted by the model with $\tau = 100$ to within experimental errors, indicating that by this stage the solid particles are out of equilibrium with the gas jet and do not move with the flow. Outside the core, comparing experimental data between the quadrants, a difference is clear between the western quadrant when compared to the eastern and northern quadrants. The southern

quadrant also shows a similar effect, albeit to a lesser degree. Given that the cross-wind is coming from the WSW, a simple explanation is that the cross-wind is strongly shifting or compressing the jet towards the axis. Considering the eastern quadrant to be the least likely affected by cross-wind then, the fit of the relaxation model predictions from a two-dimensional axisymmetric model which does not capture atmospheric effects is almost entirely to within the experimental error. The predicted width of the jet at 7m is also in agreement with the experimental data and photographs of the release.

5.2.3. Centreline predictions

Figure 8 shows model predictions along the centreline axis of the jet obtained using the homogeneous relaxation model with $\tau = 100$ and the homogeneous equilibrium model. The temperature drops quickly in the expansion fan up to the Mach shock, where it then jumps back up through the shock to the sublimation temperature (-79.9 degC), as this is the only temperature at which CO₂ gas and solid can co-exist at atmospheric pressure in pure phase equilibrium. Further downstream from the shock, as the relaxation model allows the gas temperature to diverge from the equilibrium prediction, the core temperature begins to rise. In the equilibrium model, the temperature in the core of the jet remains at or below the sublimation temperature whilst solids are present - up until approximately $x = 6.75\text{m}$ where the solid fraction drops to zero in the equilibrium prediction. The mean velocity increases rapidly to supersonic levels in the expansion fan, resulting in the Mach shock structure of the near-field expansion. At the shock it falls to mildly subsonic levels in a slow moving core surrounded by a fast moving (around 100 m s^{-1}) annulus of CO₂ mixed with air. The core gradu-

ally speeds up and reduces in size as the turbulence mixes air inwards, until a single jet structure is formed with the highest velocities on the centreline and air mixed into the core of the jet. After this point the velocity gradually decreases in the same fashion as the annulus velocity has been decreasing since the Mach shock, although even at 7m (288D) from the release point, the mean velocity is approximately 50 m s^{-1} . The fraction of CO_2 along the centreline is 100% in the expansion, through the Mach shock and in the protected slow core of the jet, until air begins to mix into the core. After that point, around 1m or approximately 40 vent diameters downstream from the release point, the fraction of CO_2 in the core of the jet begins to decrease. As this is a liquid release, the condensed phase fraction is initially 100%, as shown by the centreline plot. Any 'flashing' at the vent exit is not included in the model employed here. The measurements suggest that the release is borderline all liquid, just possibly meta-stable liquid, possibly with a very small flash (GLND; private communication). Even with flashing, however, there would be a high liquid content. Within a short distance into the expansion fan, the temperature has dropped below the triple point and hence all the condensed phase material freezes to solid phase. The point at which this occurs is just discernible very near the vertical axis in the temperature plot, as the temperature drops through -56.6 degC . The composite equation of state employed in the model results in 30% solid in the core of the jet just after the Mach shock, dropping to 10% at 8m or 325 vent diameters from the vent exit. This is considerably less than that predicted when employing a standard two-phase Peng-Robinson equation of state, but the application of which assumes no latent heat of fusion and hence instantaneous solid for-

mation with no jump in internal energy. See Wareing et al (Wareing et al., 2013) for further details. The composite model also predicts higher velocities and temperatures, so in order to correctly model the near-field dispersion of these releases, a three-phase model is required that correctly accounts for the energy changes, as there are notable differences in the predicted flow from the simpler alternatives of using a standard two-phase equation of state (Wareing et al., 2013). The final plot in Figure 8 shows the pressure along the centreline of the jet. Immediately after the Mach shock, the pressure becomes equivalent to atmospheric and remains there.

5.2.4. Near-field predictions

Figure 9 shows the near-field predictions of the dense phase test release, where near-field has the usual meaning where the flow is dispersing to atmospheric pressure. The drop in temperature can clearly be seen in the expanding fan out to the Mach shock, as can drops in pressure and density, as well as an increase in the mean velocity. The core and annulus structure is also clear in the plot of mean velocity. The plot of CO₂ fraction shows the slower core is purely CO₂ and mixing with air is occurring in the turbulent edges of the jet (the annulus). The fraction of solid is fairly uniform across the jet, although slightly higher in the annulus. Physically, the Mach shock is at a distance of 0.2m (8D) from the release point along the centreline. The shock is approximately 5D wide and encased by a turbulent mixing zone which is widened by the compressibility correct k- ϵ turbulence model. The ideal and Peng-Robinson equations of state predict considerably different near-field conditions (Wareing et al., 2012, 2013).

5.2.5. Far-field predictions

In order to compare simulated data to the experimental measurements, the conditions at 20D from the vent exit were taken as input, as shown in Figure 9, and simulated out to the distances of the measuring planes and beyond in order to avoid simulation domain effects. These conditions in the far-field of the jet are shown in Figure 10. The merger of the slower core and fast annulus around 1 to 2m (40D to 80D) downstream from the release point is clear in the mean velocity plot. The presence of solid phase material along the length of the jet also maintains its low temperature.

5.3. Gas Phase Test

5.3.1. 4m and 7m measurement planes

In Figures 11 and 12 the model predictions and the experimental data are shown for the gas phase vertical vent release test performed with a 0.0243m internal diameter vent pipe. It should be noted that in the gas phase test, no condensed phase material is present in the flow and so we do not show predictions with varying values of the τ parameter as this has no relevance here. We have confirmed this by obtaining identical predictions with $\tau = 100, 1000$ and $10,000$. Figures 11 and 12 show the model predictions compared to the quadrants of experimental data from the planes 4m and 7m above release point, respectively. The experimental temperatures are close to atmospheric in both cases. The predictions are in reasonably good agreement with the data, particularly in the core. The predicted temperatures are possibly on average less than the observations, but the widths are in good agreement. At 7m, there is arguably a wind effect in the western quadrant. Considering the eastern quadrant then, the fit to the experimental data is within experimen-

tal errors. We have noted differences when achieving steady state with this model from a sonic jet release. We have shown the results from the calculations that provide the best fit to the experimental data. All predictions are convergent, demonstrating the reliability of the model. The differences are minimal, specifically the core temperatures are virtually the same, although the position of the predicted peak (indicating the width of the jet) varies from $r=0.8\text{m}$ to that shown at $r=0.95\text{m}$ at the 4m plane, and $r=1\text{m}$ to that shown at $r=1.4\text{m}$ at the 7m plane.

5.3.2. Centreline predictions

Figure 13 shows the centreline predictions along the axis of the jet. Whilst the Mach shock structure is still present, with exceptionally high velocities and low temperatures, the structure beyond the Mach shock is considerably different with no condensed phase component, i.e. a gas phase release does not result in solid particles in the dispersing flow in this case.

5.3.3. Near-field predictions

Figure 14 shows the two-dimensional predictions of the gas phase test. The Mach shock is much narrower than in the case of the dense phase release, with faint shock diamonds further downstream. The core and annulus structure is rapidly subsumed by the turbulent jet flow, as is evident in the mean velocity plot. Again, though, the core of the jet is purely CO_2 until outside the domain shown here: 10D (0.25m) radially and 15D along the axis (0.375m).

5.3.4. Far-field predictions

Figure 15 shows the far-field model predictions for the gas phase test. As expected, without solids the temperature (top left) rapidly rises and the mean velocity rapidly drops. Within a relatively short distance of the release point - 100D or 2.5m - the concentration of CO₂ rapidly drops below 25% and reduces to low levels (3%) by the edge of the domain. Density has been displayed logarithmically to show there is a definite edge to the jet, which is not clearly detected in the experimental data. Given that the gas phase jet carries considerably less momentum (see Table 1 for the velocities and densities), atmospheric flows are likely to have had an effect on the gas phase jet. Applying the axisymmetric model to this experimental data, particularly at the second measuring plane, indicates that clearly a full three-dimensional model accounting for cross-winds is required.

6. Discussion

The comparisons presented in the previous section have shown that the composite equation of state (Wareing et al., 2012, 2013) can predict the characteristics of high pressure releases of CO₂ from reservoir conditions similar to those under consideration in the Carbon Capture and Storage industry. The two-dimensional axisymmetric model, with a homogeneous relaxation model, can predict the near-field structure of a free jet released into the atmosphere resulting in accurate core temperatures and other jet characteristics further downstream. The fit of the predictions to the experimental data demonstrates the need for a complex equation of state in the near-field. This approach needs to not only account for accurate behaviour in the gas

and liquid phases, but also the solid phase and the transitional latent heat of fusion, since the temperatures rapidly drop below the triple point in the release. The two-dimensional axisymmetric model does encounter problems modelling away from the near-field when a cross-wind is present. These issues can be addressed by a full three-dimensional model, which is under development, coupled to improved turbulence modelling. To obtain good fits to the experimental data, the model currently requires a homogeneous relaxation model which allows the solid particles to be out of equilibrium with the gas phase. Scaling these results up to full-scale pipeline releases indicates that solid CO₂ will be present at considerable distances from the pipeline puncture or rupture, e.g. for a 0.6m pipeline, an unhindered full-bore release into free air above ground would contain solid CO₂ (at a level of 10% of the CO₂ fraction) at 200m from the rupture. This extrapolation is based on steady pressure at the outflow of the pipe, which in a full-bore is not realistic - the pressure would in fact drop very rapidly. Nevertheless, considerable amounts of solid will be present in the flow. Burying a pipeline will likely confine the solid CO₂ that might be released following a puncture or rupture within and around the crater formed by the release, but that introduces a further problem of an amount of solid CO₂ in a confined area. Hazard analyses will need to take these effects into account.

The introduction of water vapour into the flow will make a difference. Centreline predictions indicate the jet is entirely CO₂ until approximately 40 release diameters downstream from the release point for liquid phase releases, and approximately 20 diameters downstream for a gas phase release. Any water vapour in the air cannot affect the core of the jet whilst it is 100%

CO₂, so it is unlikely to have an effect on the near-field around the Mach shock as that is always within 10 diameters of the release point. Once air does begin to mix into the jet core, water ice will form in the low temperature environment and, since water has a latent heat of fusion approximately five times greater than that of CO₂, it will act as an energy sink causing the CO₂ jet to be less cold (on the order of a few degrees at most, depending on the level of humidity). The jet formed will also be more buoyant. Thus it is possible that including the effect of water vapour is a mechanism likely to rectify the final few degrees difference between the current predictions and experimental data, and may also slightly relax the requirement to go as far out of equilibrium in the jet. This will be investigated in future work.

Another source of uncertainty is in the input conditions. Whilst these are reasonably well confined by experimental measurements in the pipework, there is some experimental evidence for phase disequilibrium at the outlet. We employ outlet conditions that are in homogeneous equilibrium at the outlet, but then find that the only way to fit experimental measurements in the flow field is to go out of equilibrium, indicating that future work should examine this in more detail.

7. Conclusions

This article has presented the testing and validation of a novel two-dimensional near-field dispersion model against an experimental dataset obtained as part of the COOLTRANS programme of research (Cooper, 2012). The model has proved capable of accurately predicting the near-field Mach shock structure, and into the far-field, the core and radial temperatures across

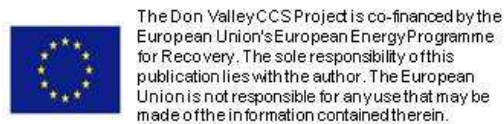
jets formed by high pressure releases of CO₂ to the atmosphere. This has required a three-phase accurate equation of state, that also accounts for the latent heat of fusion, as well as a homogeneous relaxation model to allow the modelling of out-of-equilibrium effects. Further improvements to the model may remove the necessity for a relaxation model, but it is clear the complex equation of state is required to obtain the best predictions of near-field dispersion. To allow modelling of cross-winds in the atmospheric boundary layer that can clearly affect such releases, a fully three-dimensional model is required. It is also likely that a more complete treatment of these data, and other data that has become available for model validation, e.g. from the CO2PIPETRANS project, will require a two-way coupled flow and a non-equilibrium particle model that includes evolution of solid particles and effects such as turbulent agglomeration and evaporation/sublimation.

In order to provide a more accurate prediction of the jet temperatures (we have considered up to 300D here) this sophisticated model is required. The model validated here provides a robust basis for the definition of simple equivalent sources for use with a less sophisticated modelling approach, although there will inevitably be some loss of detail when these are defined. The importance of this loss of detail is not investigated in this paper, but the results presented in this article allow for the subsequent development and testing of possible source approaches. For example, as an alternative to the present modelling approach, if one chooses a particular distance downstream where a pseudo-source is to be defined, it should now be possible to adjust that pseudo-source to give an adequate representation of the reality presented here (i.e. the levels of solid phase material in the jet and the complex slow

core and fast annulus structure). Such a source would allow for the accurate influence of near-field effects on subsequent far-field dispersion predictions.

Acknowledgements

CJW was supported by the COOLTRANS Research Programme (Cooper, 2012) funded by National Grid Plc, and CJW and MF would like to thank National Grid for their support of the work described herein. National Grid has initiated the COOLTRANS programme of research to address knowledge gaps relating to the safe design and operation of onshore pipelines for transporting dense phase CO₂ from industrial emitters in the UK to storage sites offshore. We acknowledge the provision of information regarding the experiments from GLND (D. Allason, K. Armstrong and R.P. Cleaver) and of input conditions from UCL (A. Collard, S. Brown and H. Mahgerefteh).



References

- Allason, D., Armstrong, K., Cleaver, P., Halford, A., Barnett, J., 2012. Experimental studies of the behaviour of pressurised release of carbon dioxide, in: IChemE Symposium Series No. 158, IChemE. pp. 142–152.
- Cooper, R., 2012. National Grid's COOLTRANS research programme. *Journal of Pipeline Engineering* 11, 155–172.

- Cumber, P.S., Fairweather, M., Falle, S.A.E.G., Giddings, J.R., 1994. Predictions of the structure of turbulent, moderately underexpanded jets. *Journal of Fluids Engineering* 116, 707–713.
- Cumber, P.S., Fairweather, M., Falle, S.A.E.G., Giddings, J.R., 1995. Predictions of the structure of turbulent, highly underexpanded jets. *Journal of Fluids Engineering* 117, 599–604.
- Dixon, C.M., Gant, S.E., Obiorah, C., Bilio, M., 2012. Validation of dispersion models for high pressure carbon dioxide releases, in: *ICHEME Symposium Series No. 158, IChemE*. pp. 153–163.
- Dixon, C.M., Hasson, M., 2007. Calculating the release and dispersion of gaseous, liquid and supercritical CO₂, in: *IMEchE Seminar on Pressure Release, Fires and Explosions*, London, IMechE.
- Dixon, C.M., Heynes, O., Hasson, M., 2009. Assessing the hazards associated with release and dispersion of liquid carbon dioxide on offshore platforms, in: *8th World Congress of Chemical Engineering*, Montreal.
- Falle, S.A.E.G., 1991. Self-similar jets. *Monthly Notices of the Royal Astronomical Society* 250, 581–596.
- Falle, S.A.E.G., 2005. AMR applied to non-linear elastodynamics, in: Plewa, T., Linde, T., Weirs, V.G. (Eds.), in the *Proceedings of the Chicago Workshop on Adaptive Mesh Refinement Methods*, Springer Lecture Notes in Computational Science and Engineering v.41, Springer, New York U.S.A.. pp. 235–253.

- Godunov, S.K., 1959. A difference scheme for numerical computation of discontinuous solutions of equations of fluid dynamics. *Math. Sbornik* 47, 271–306.
- Harten, A., Lax, P.D., van Leer, B., 1983. On upstream differencing and Godunov-type schemes for hyperbolic conservation laws. *SIAM Review* 25, 35–61.
- Hill, T.A., Fackrell, J.E., Dubal, M.R., Stiff, S.M., 2011. Understanding the consequences of CO₂ leakage downstream of the capture plant. *Energy Procedia* 4, 2230–2237.
- Hulsbosch-Dam, C.E.C., Spruijt, M.P.N., Necci, A., Cozzani, V., 2012a. An approach to carbon dioxide particle distribution in accidental releases. *Chemical Engineering Transactions* 26, 543–548.
- Hulsbosch-Dam, C.E.C., Spruijt, M.P.N., Necci, A., Cozzani, V., 2012b. Assessment of particle size distribution in CO₂ accidental releases. *J. Loss Prevention in the Process Industries* 25, 254–262.
- Jacobson, M.Z., 1999. *Fundamentals of Atmospheric Modelling*. Second ed., Cambridge University Press, Cambridge U.K.
- Liu, Y., Calvert, G., Ghadiri, C.H.M., Matsusaka, S., 2012a. Size measurement of dry ice particles produced from liquid carbon dioxide. *Journal of Aerosol Science* 48, 1–9.
- Liu, Y., Calvert, G., Hare, C., Ghadiri, M., Matsusaka, S., 2012b. Size measurement of dry ice particles produced from liquid carbon dioxide. *Journal of Aerosol Science* 48, 1–9.

- Mazzoldi, A., Hill, T., Colls, J.J., 2008a. CFD and Gaussian atmospheric dispersion models: a comparison for leak from carbon dioxide transportation and storage facilities. *Atmos. Environ.* 42, 8046–8054.
- Mazzoldi, A., Hill, T., Colls, J.J., 2008b. CO₂ transportation for carbon capture and storage: sublimation of carbon dioxide from a dry ice bank. *International Journal of Greenhouse Gas Control* 2, 210–218.
- Mazzoldi, A., Hill, T., Colls, J.J., 2011. Assessing the risk for CO₂ transportation within CCS projects, CFD modelling. *International Journal of Greenhouse Gas Control* 5, 816–825.
- Peng, D.Y., Robinson, D.B., 1976. A new two-constant equation of state. *Industrial and Engineering Chemistry: Fundamentals* 15, 59–64.
- Sarkar, S., Erlebacher, G., Hussaini, M.Y., Kreiss, H.O., 1991. The analysis and modelling of dilatational terms in compressible turbulence. *Journal of Fluid Mechanics* 227, 473–493.
- Span, R., Wagner, W., 1996. A new equation of state for carbon dioxide covering the fluid region from the triple-point temperature to 1100 K at pressures up to 800 MPa. *Journal of Physical and Chemical Reference Data* 25, 1509–1596.
- van Leer, B., 1977. Towards the ultimate conservative difference scheme. iv. a new approach to numerical convection. *Journal of Computational Physics* 23, 276–299.
- Wareing, C., Fairweather, M., Falle, S.A.E.G., Woolley, R.M., 2012.

- Reynolds-averaged Navier-Stokes modelling of sonic CO₂ jets, in: Hanzalic, K., Nagano, Y., Borello, D., Jakirlic, S. (Eds.), in the Proceedings of the 7th International Symposium on Turbulence, Heat and Mass Transfer, Begell House Inc., New York. pp. 349–512.
- Wareing, C., Woolley, R.M., Fairweather, M., Falle, S.A.E.G., 2013. A composite equation of state for the modelling of sonic carbon dioxide jets in carbon capture and storage scenarios. *AIChE* 59, 3928–3942.
- Webber, D.M., 2011. Generalising two-phase homogeneous equilibrium pipeline and jet models to the case of carbon dioxide. *J. Loss Prevention in the Process Industries* 24, 356–360.
- Witlox, H.W.M., Harper, M., Oke, A., 2009. Modelling of discharge and atmospheric dispersion for carbon dioxide release. *J. Loss Prevention in the Process Industries* 22, 795–802.
- Witlox, H.W.M., Stene, J., Harper, M., Nilsen, S.H., 2011. Modelling of discharge and atmospheric dispersion for carbon dioxide releases including sensitivity analysis for wide range scenarios. *Energy Procedia* 4, 2253–2260.
- Woolley, R.M., Fairweather, M., Wareing, C.J., Falle, S.A.E.G., Proust, C., Hebrard, J., Jamois, D., 2013. Experimental measurement and Reynolds-averaged Navier-Stokes modelling of the near-field structure of multi-phase CO₂ jet releases. *IJGGC* 18, 139–149.

Notation

Roman letters:

a	model parameter
b	model parameter
c	adiabatic sound speed
C	specific heat
d	non-dimensional nozzle diameter
e	total energy per unit volume
F	Helmholtz free energy
k	turbulence kinetic energy
m	mass
p	pressure
r	non-dimensional radial location
R	universal gas constant
t	time
S	entropy
T	temperature
u	magnitude of velocity
U	internal energy per unit mass
v	molar volume
w	molecular weight
z	non-dimensional axial location

Greek letters:

α	condensed phase fraction
β	total mass fraction of CO ₂
δ	Peng-Robinson equation of state parameter
ϵ	dissipation rate of k
γ	ratio of specific heats
μ	molecular viscosity
ρ	density
τ	relaxation time
ω	acentric factor of the species

Subscripts:

0	reference state
a	air
c	condensed phase
crit	critical point
g	gas
i	initial
mix	mixture
s	saturation
trip	triple point
v	vapour

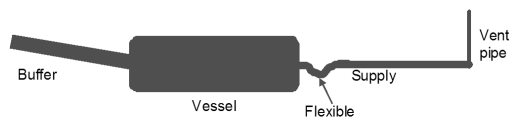


Figure 1: Schematic of experimental rig. (Courtesy of GLND)



Figure 2: View of vertical vent pipe, held in place by a tripod support, on the left and on the right a view of the experimental array structure during a test release. (Courtesy of GLND)

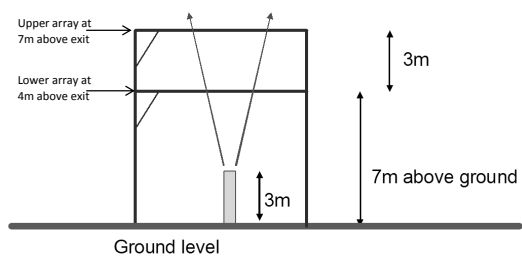


Figure 3: Location of horizontal planes above the vent pipe in which temperature measurements were made in the releases. (Courtesy of GLND)

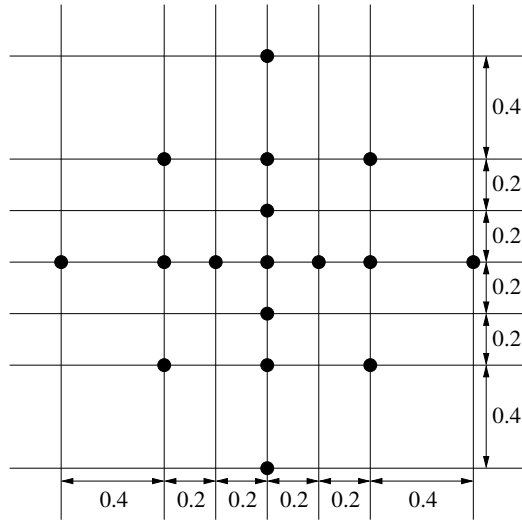


Figure 4: The central section of the lower array, 7m above the ground. Circular markers indicate the position of temperature sensors. (Courtesy of GLND)

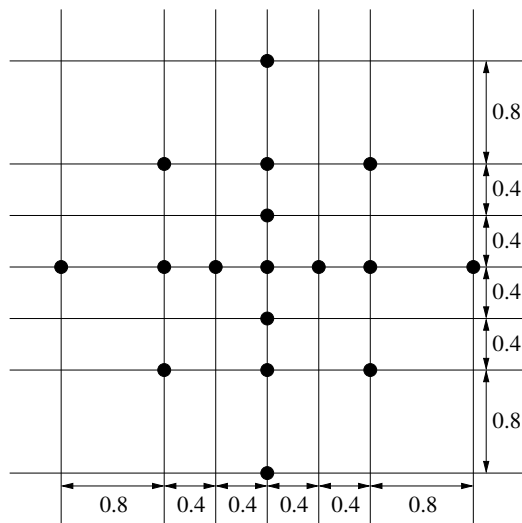


Figure 5: The central section of the upper array, 10m above the ground. Circular markers indicate the position of temperature sensors. (Courtesy of GLND)

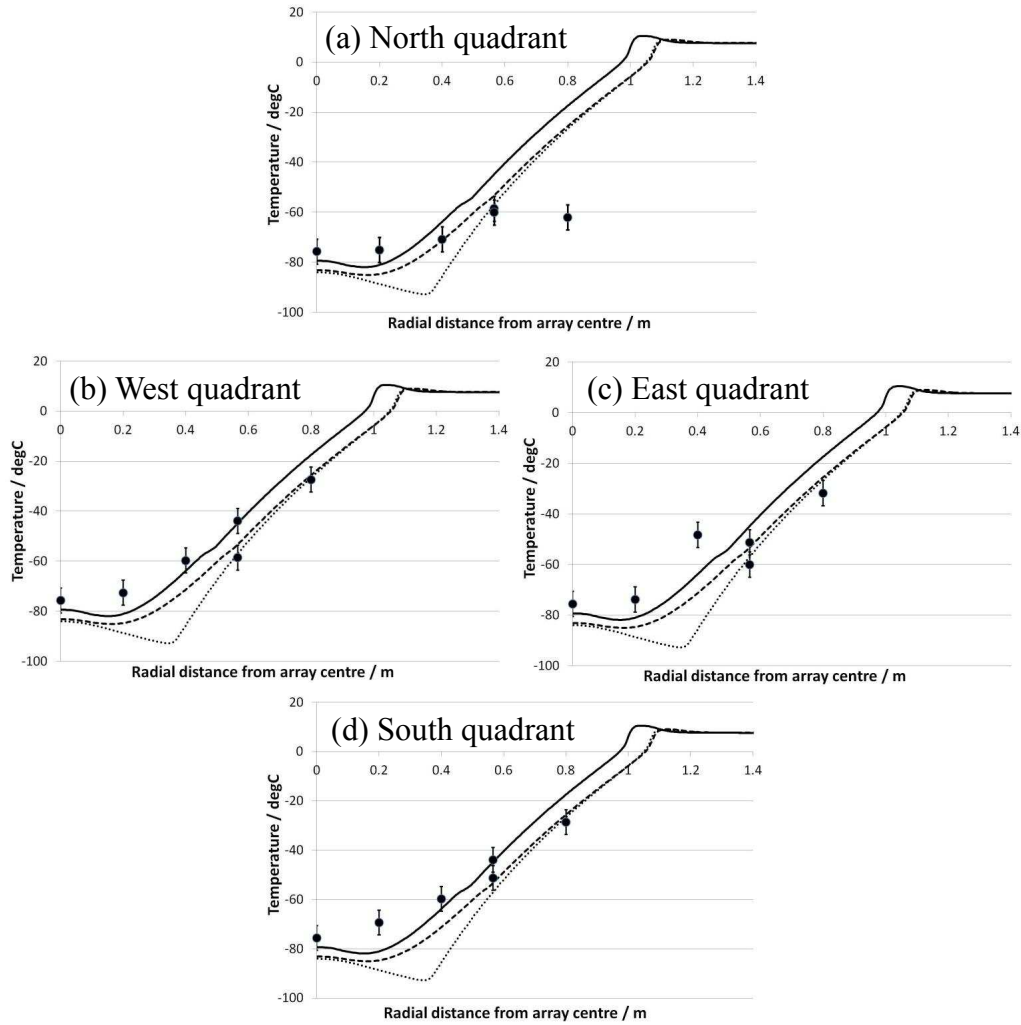


Figure 6: Dense phase test 4m plane experimental measurements (Allason et al., 2012) and equilibrium (dotted line), $\tau = 10$ (dashed line) and $\tau = 100$ (solid line) model predictions; (a) North quadrant, (b) West quadrant, (c) East quadrant, (d) South quadrant. The cross-wind is from the west, left to right across the middle row. A feel for the data scatter caused by the cross-wind can be obtained by considering the temperature measurements at specific radial distances and comparing between these four plots. Section 5.1 presents a full explanation of these figure geometries.

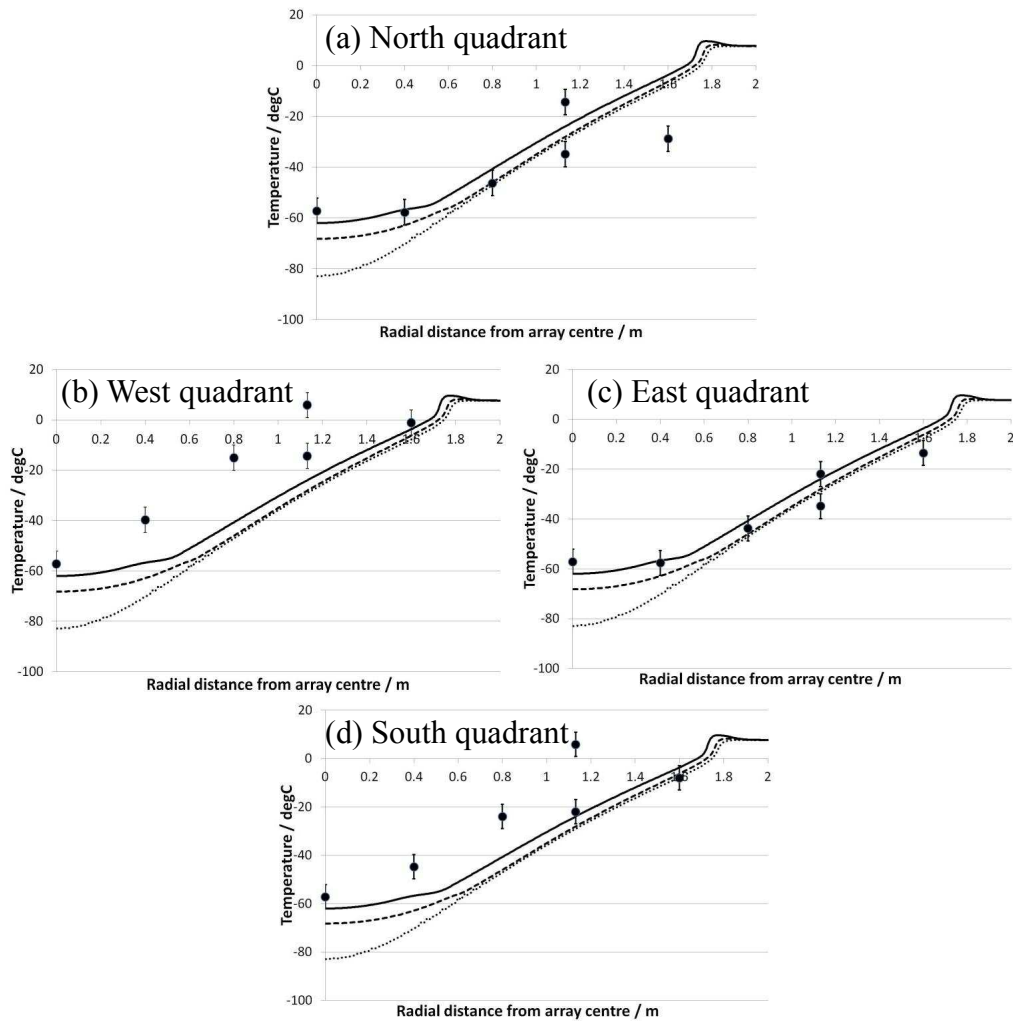


Figure 7: Dense phase test 7m plane experimental measurements (Allason et al., 2012) and equilibrium (dotted line), $\tau = 10$ (dashed line) and $\tau = 100$ (solid line) model predictions; (a) North quadrant, (b) West quadrant, (c) East quadrant, (d) South quadrant. The cross-wind is from the west, left to right across the middle row. A feel for the data scatter caused by the cross-wind can be obtained by considering the temperature measurements at specific radial distances and comparing between these four plots. Section 5.1 presents a full explanation of these figure geometries.

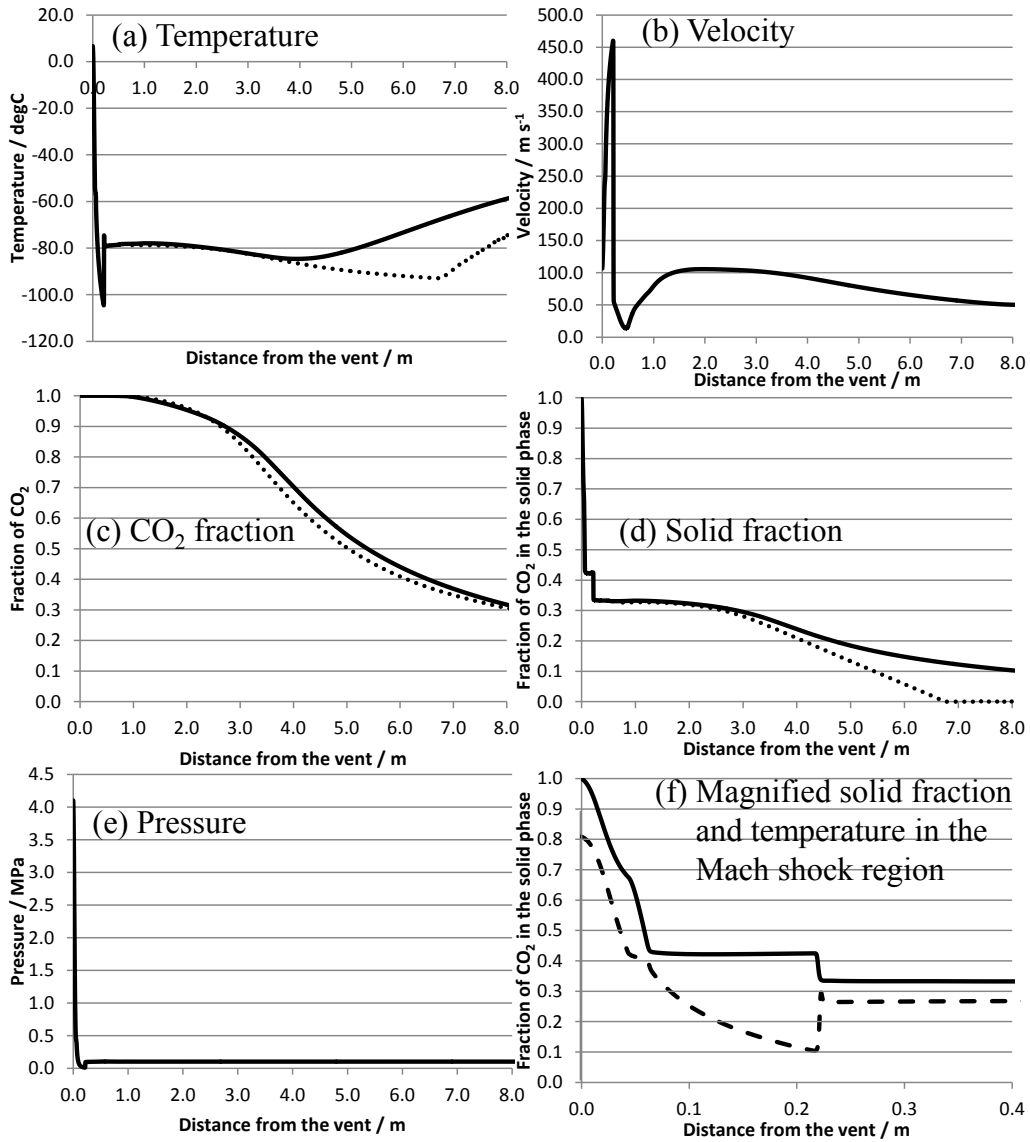


Figure 8: Dense phase test model predictions along the centreline of the jet for the $\tau = 100$ relaxation model (solid line) and the equilibrium model (dotted line); (a) temperature, (b) mean velocity, (c) CO₂ fraction, (d) fraction of CO₂ in the solid phase and (e) pressure. The equilibrium prediction is only shown where a relevant difference is observed between the predictions. In the final panel (f), a magnified region of CO₂ fraction (solid line) is shown with temperature (dashed line) scaled over the top on the same x range, in order to highlight the passage through the triple point at approximately $x = 0.5$ m, whereupon the solid fraction is then approximately 0.42 until the Mach shock at $x = 0.22$ m.

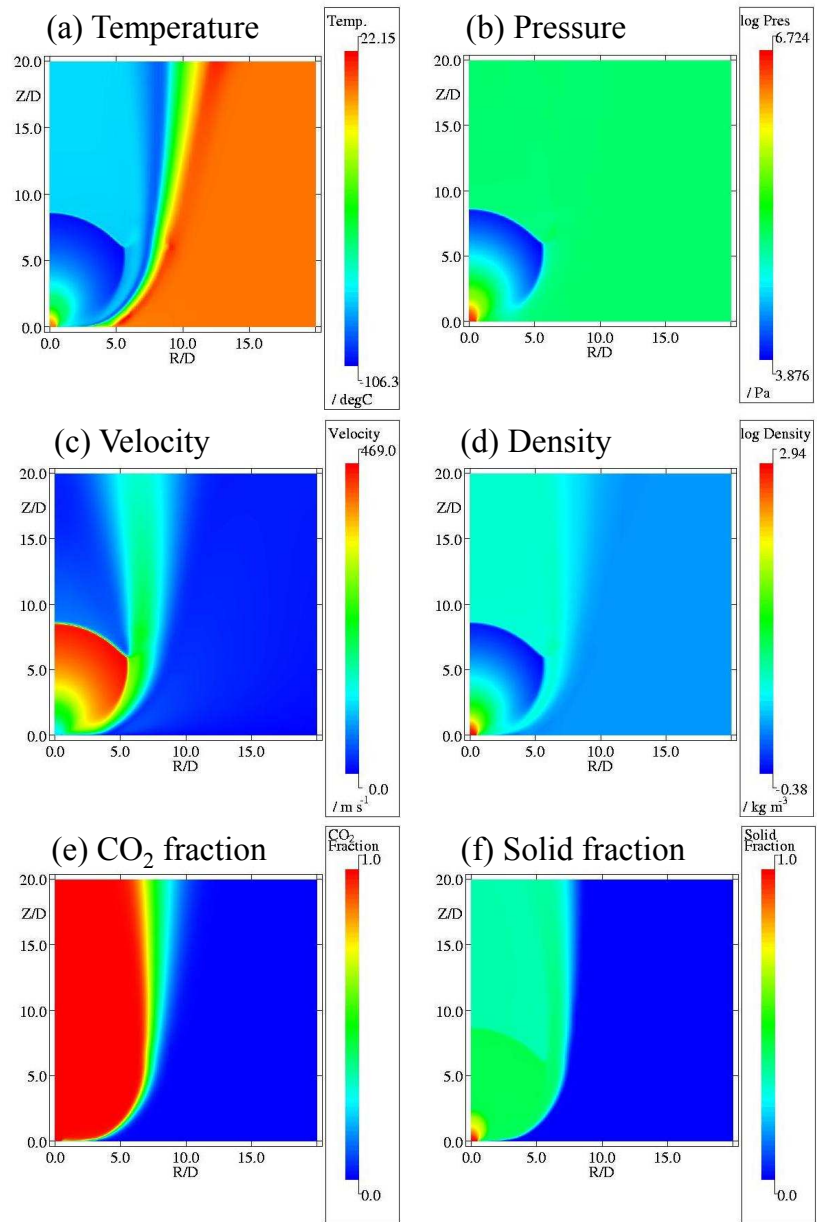


Figure 9: Dense phase test near-field predictions; (a) temperature, (b) the logarithm of the pressure, (c) mean velocity, (d) the logarithm of the density, (e) CO₂ fraction and (f) the fraction of CO₂ in the solid phase. Axes are scaled in units of the vent exit diameter. The extent of the square domains shown here are hence 0.5m by 0.5m.

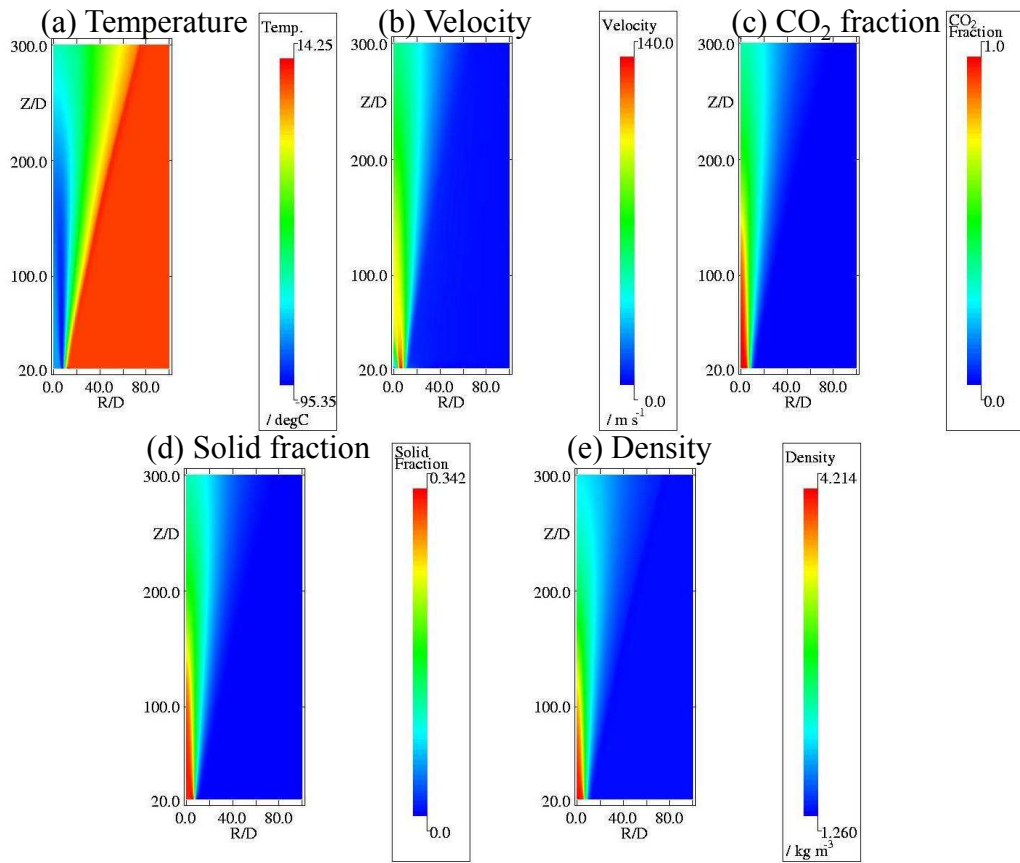


Figure 10: Dense phase test far-field predictions; (a) temperature, (b) mean velocity, (c) CO₂ fraction, (d) fraction of CO₂ in the solid phase and (e) density. Pressure is not shown as it is uniformly at atmospheric pressure throughout the domain.

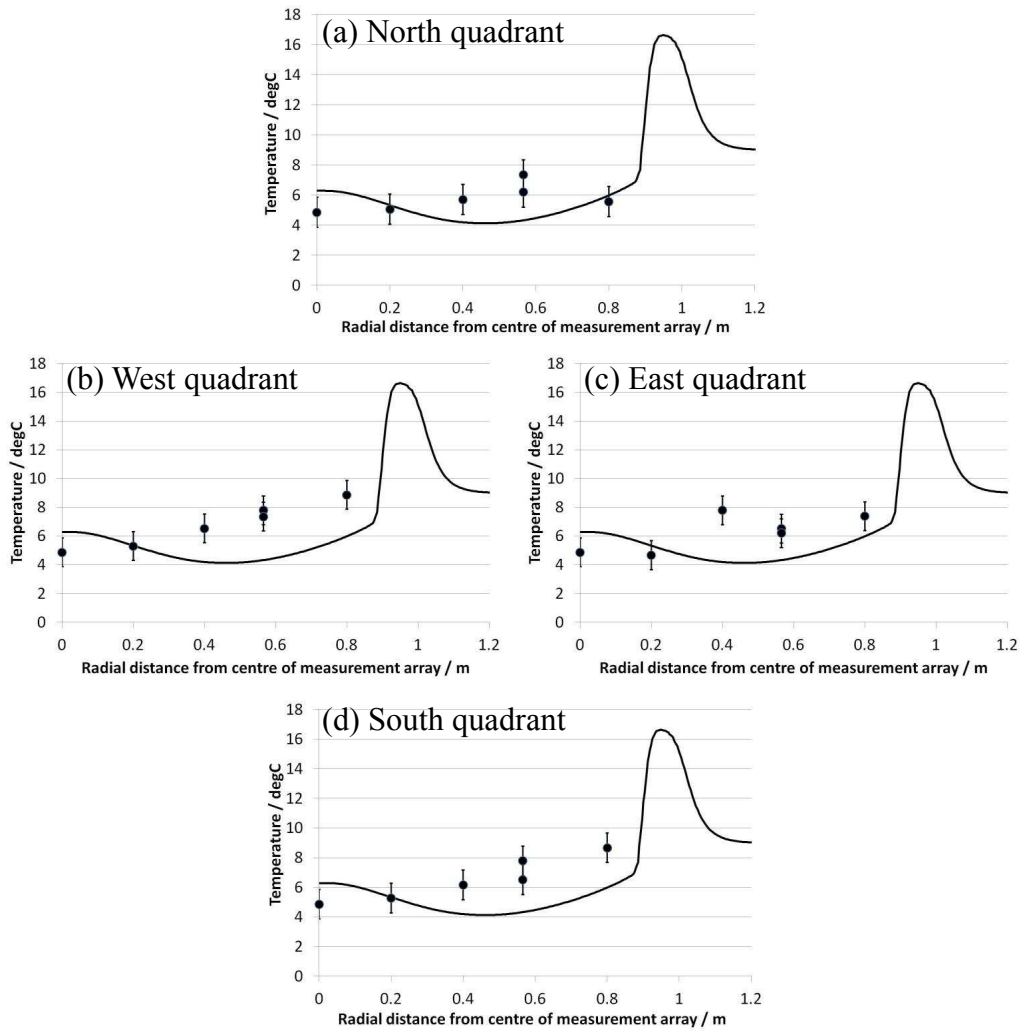


Figure 11: Gas phase test 4m plane experimental measurements (Allason et al., 2012) and model predictions; (a) North quadrant, (b) West quadrant, (c) East quadrant, (d) South quadrant. The cross-wind is from the west, left to right across the middle row. Section 5.1 presents a full explanation of these figure geometries.

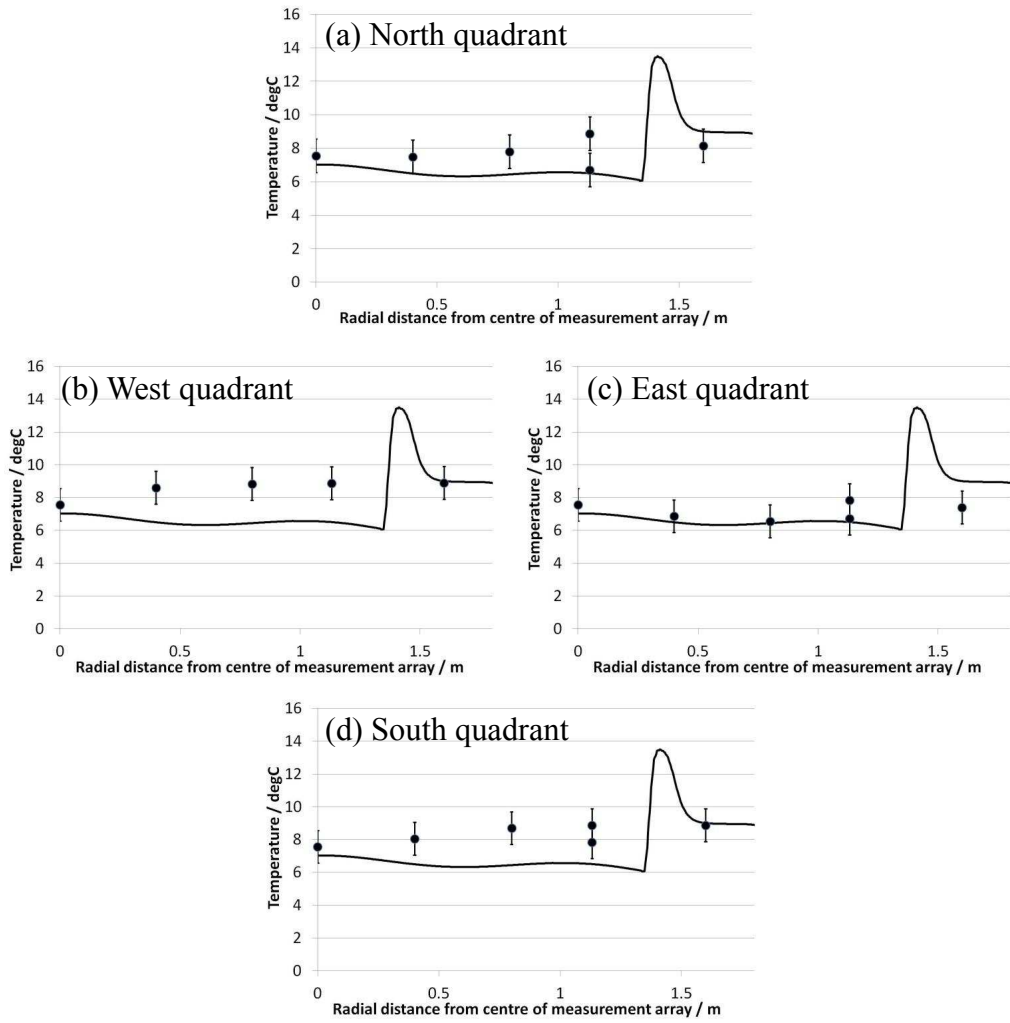


Figure 12: Gas phase test 7m plane experimental measurements (Allason et al., 2012) and model predictions. (a) North quadrant, (b) West quadrant, (c) East quadrant, (d) South quadrant. The cross-wind is from the west, left to right across the middle row. Section 5.1 presents a full explanation of these figure geometries.

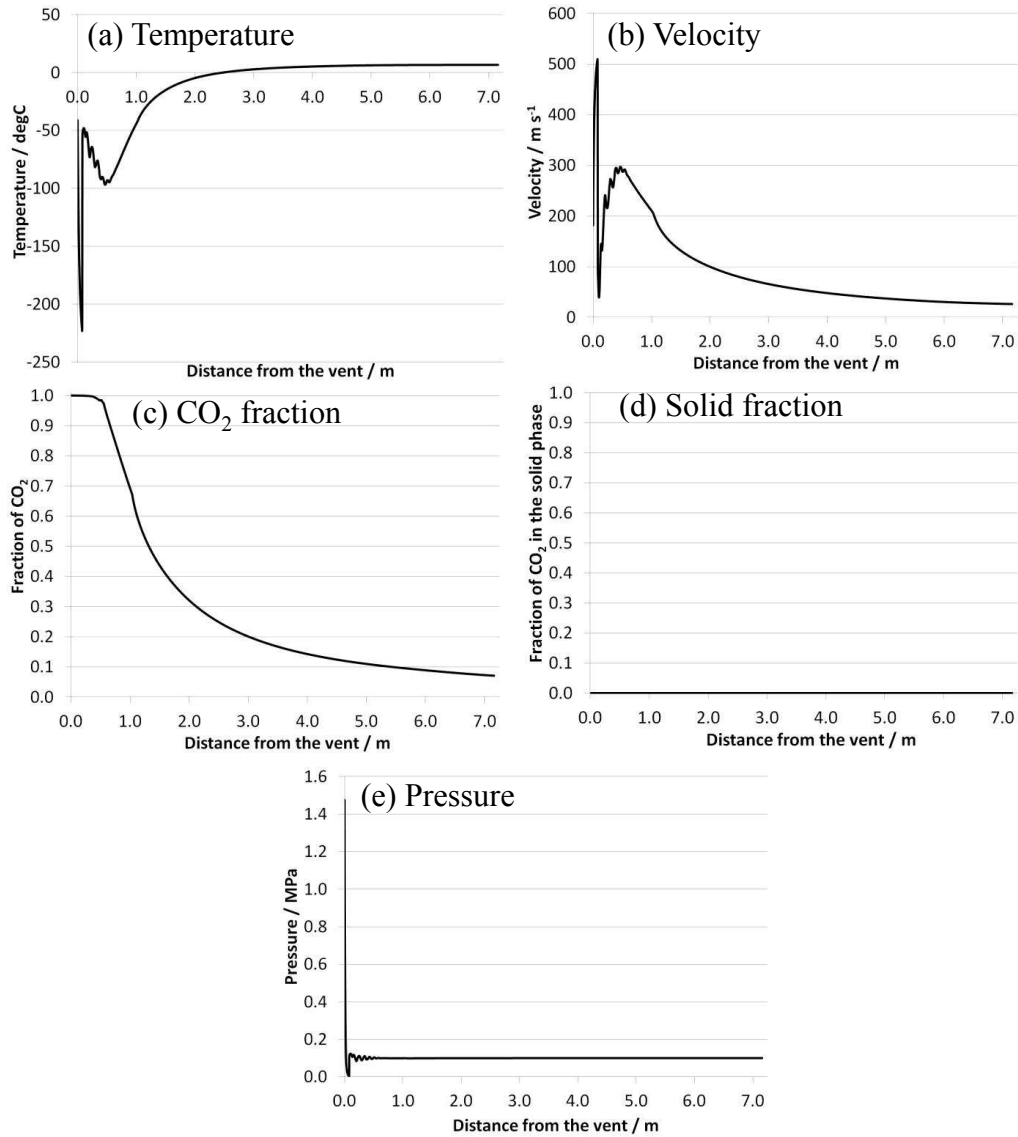


Figure 13: Gas phase test model predictions along the centreline of the jet for the $\tau = 100$ relaxation model; (a) temperature, (b) mean velocity, (c) CO₂ fraction, (d) fraction of CO₂ in the solid phase (zero throughout) and (e) pressure.

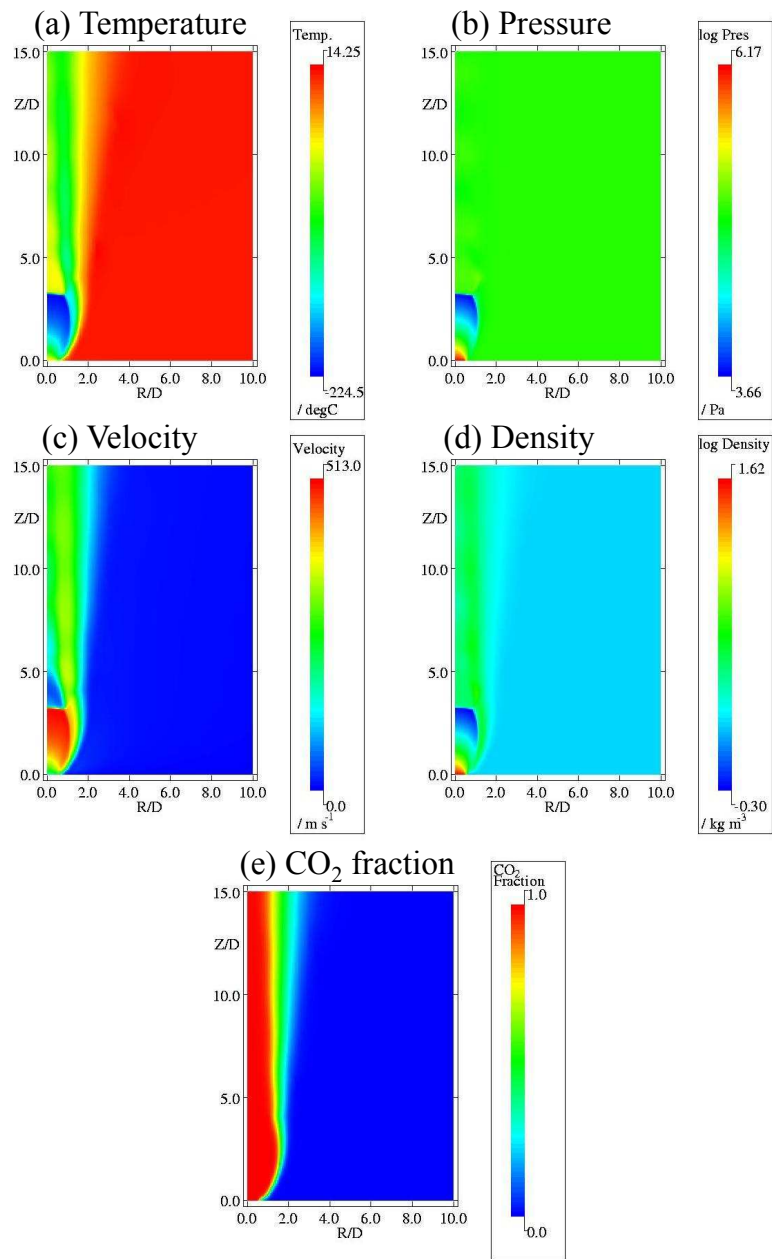


Figure 14: Gas phase test near-field predictions; (a) temperature, (b) the logarithm of the pressure, (c) mean velocity, (d) the logarithm of the density and (e) CO₂ fraction. Axes are scaled in units of the vent exit diameter. The extent of the domains shown here is then 0.375m along the axis by 0.25m radially.

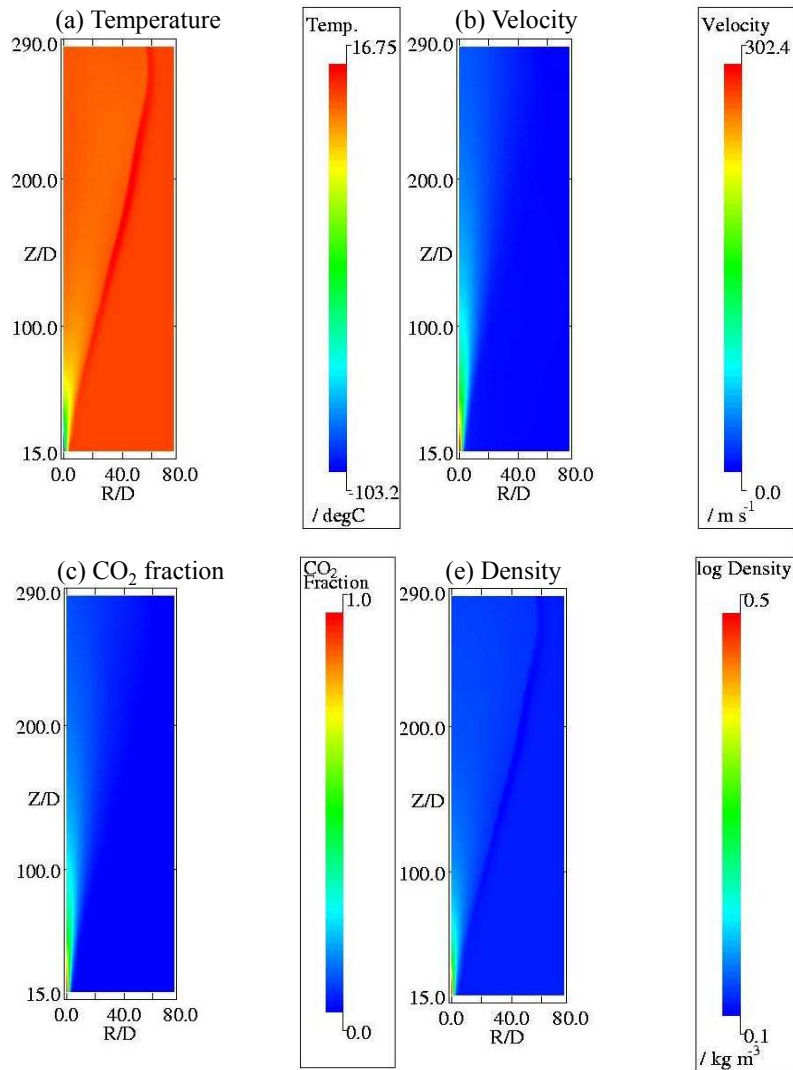


Figure 15: Gas phase test far-field model predictions; (a) temperature, (b) mean velocity, (c) CO₂ fraction and (d) the logarithm of the density. Pressure is not shown as it is uniformly at atmospheric pressure throughout the domain and there is no condensed phase CO₂.

Table 1: Initial conditions for tests considered here.

Reservoir conditions (Courtesy of GLND)	Dense phase test	Gas phase test
Pressure	15.00 MPa	3.55 MPa
Temperature	7.45 degC	8.75 degC
CO ₂ fraction	1.00	1.00
Condensed phase fraction	1.00	0.00
Atmospheric conditions (Courtesy of GLND)	Dense phase test	Gas phase test
Pressure (P_a)	0.1 MPa	0.1 MPa
Temperature (T_a)	7.45 degC	8.75 degC
Velocity (u_a)	2.77 m s ⁻¹	5.74 m s ⁻¹
Wind bearing	251.95 degrees	257.60 degrees
Predicted vent-pipe exit plane conditions (Courtesy of UCL)	Dense phase test	Gas phase test
Pressure (P_i)	4.14 MPa	1.969 MPa
Temperature (T_i)	6.85 degC	-19.31 degC
Mean velocity (u_i)	105.60 m s ⁻¹	127.90 m s ⁻¹
CO ₂ fraction (β_i)	1.00	1.00
Liquid fraction (α_i)	0.99	0.00
Liquid density (ρ_l)	883.58 kg m ⁻³	n/a
Gas density (ρ_g)	121.45 kg m ⁻³	54.22 kg m ⁻³
Density (ρ_i)	831.41 kg m ⁻³	54.22 kg m ⁻³